Front. Earth Sci. 2020, 14(2): 430–445
https://doi.org/10.1007/s11707-019-0785-5

RESEARCH ARTICLE

Exploring the influence of various factors on microwave radiation image simulation for Moon-based Earth observation

Linan YUAN[1,2], Jingjuan LIAO (✉)[1]

1 Key Laboratory of Digital Earth Science, Aerospace Information Research Institute, Chinese Academy of Sciences, Beijing 100094, China
2 University of Chinese Academy of Sciences, Beijing 100049, China

Abstract Earth observation technologies are important for obtaining geospatial information on the Earth's surface and are used widely in many disciplines, such as resource surveying, environmental monitoring, and evolutionary studies. However, it is a challenge for existing Earth observation platforms to acquire this type of data rapidly on a global scale due to limitations in orbital altitude and field of view; thus development of an advanced platform for Earth observation is desirable. As a natural satellite of the Earth, placement of various sensors on the Moon could possibly facilitate comprehensive, continuous, and long-term observations of the Earth. This is a relatively new concept and the study is still at the preliminary stage with no actual Moon-based Earth observation data available at this time. To understand the characteristics of Moon-based microwave radiation, several physical factors that potentially influence microwave radiation imaging, e.g., time zone correction, relative movement of the Earth-Moon, atmospheric radiative transfer, and the effect of the ionosphere, were examined. Based on comprehensive analysis of these factors, the Moon-based microwave brightness temperature images were simulated using spaceborne temperature data. The results show that time zone correction ensures that the simulation images may be obtained at Coordinated Universal Time (UTC) and that the relative movement of the Earth-Moon affects the positions of the nadir and Moon-based imaging. The effect of the atmosphere on Moon-based observation is dependent on various parameters, such as atmospheric pressure, temperature, humidity, water vapor, carbon dioxide, oxygen, the viewing zenith angle and microwave frequency. These factors have an effect on atmospheric transmittance and propagation of upward and downward radiation. When microwaves propagate through the ionosphere, the attenuation is related to frequency and viewing zenith angle. Based on initial studies, the simulation results suggest Moon-based microwave radiation imaging is realistic and viable.

Keywords Moon-based Earth observation, microwave brightness temperature simulation, relative movement of Earth-Moon, atmospheric radiative transfer, ionosphere

1 Introduction

At present, remote sensing is the accepted way to conduct high-precision and large-scale Earth observation and has been used to monitor the resources and environmental changes on the Earth. Existing airborne and spaceborne platforms cannot rapidly acquire the observation data on a global basis due to a low orbital altitude, a limited field of view, and a long revisiting cycle. Although image fusion and mosaic can expand the coverage, the results cannot satisfy the demands for spatial and temporal consistency in global observation owing to the different acquisition times. In addition, Earth observation satellites cannot acquire long-term and stable Earth observation data due to their short lifetimes. Hence, it is necessary to devise a new observation platform to ensure improvement in Earth observation capability.

Since the 21st century, a number of lunar exploration programs have been launched with a view of returning to the Moon to set up a large-scale lunar base. Researchers have thus begun to pay more attention to Moon-based Earth observations. As a new method for Earth observation, Moon-based Earth observation offers unique advantages when compared with artificial satellites, such as long platform life, expanded coverage, multi-sensor capability, and continuous Earth observation. (Guo et al., 2014). As a result, Moon-based sensors can potentially be applied across a range of subjects including solid Earth dynamics,

Received August 30, 2018; accepted August 9, 2019

E-mail: liaojj@radi.ac.cn

energy budgets, the Earth's environmental systems, and the Earth-space environment (Guo et al., 2018).

Theoretical research concerning Moon-based Earth observation is in its preliminary stages with numerous studies focusing on the feasibility and performance of Moon-based Earth observation platforms. Using the data from Apollo 15, Huang (2004, 2008) showed that the surface temperature of the Moon (the side facing the Earth) accurately records important information about the Earth's climate system. Hamill (2007) evaluated the advantages and feasibility of Moon-based Earth observations and found that a panoramic view of the Earth can be obtained from the side of the Moon closest to the Earth's surface. Based on comprehensive analysis, Johnson et al. (2007) articulated the scientific rationale for Moon-based Earth observations using visible and near-infrared instrumentation, and examined various factors, such as spatial, spectral, and temporal resolution. Fornaro et al. (2010) analyzed the performance and potential applications of spaceborne and Moon-based synthetic aperture radar (SAR) systems. Zhang (2012) calculated the real-time Earth-Moon orbital position under the Cartesian solar centroid coordinate system using the ephemeris data from the Jet Propulsion Laboratory (JPL). Ding et al. (2014) discussed several advantages of a Moon-based SAR system superior to a low Earth orbit and its possible applications. Guo et al. (2016) analyzed the Moon-based SAR system parameters, including the visual range, observable days, spatial resolution and swath width, and discussed the characteristics of the lunar platform and Moon-based sensors, as well as the scientific objectives for Moon-based Earth observation and potential applications. Ye et al. (2016) conducted coverage analysis of Moon-based Earth observation using the JPL ephemeris data and generated observation Boolean matrixes of sensitive regions for global change. The results showed that Moon-based Earth observation offers advantages for monitoring and understanding of global change due to its wide swath, continuous observation, and large coverage. Ren et al. (2017) developed a simulation system for Moon-based Earth observations and reference system transformations using the JPL ephemerides data.

At present, research on Moon-based Earth observation is still in its preliminary stage without actual observation data. To better understand the characteristics of a Moon-based microwave radiation and support its system design, a Moon-based microwave radiation imaging simulation was undertaken. First, several factors that could potentially influence the performance of a Moon-based microwave radiation imaging system (e.g., time zone correction, relative movement of the Earth-Moon, atmospheric radiative transfer, the effect of the ionosphere) were examined. Moon-based microwave radiation images were then simulated using temperature data obtained by satellite and the simulation results were then validated with existing satellite microwave radiation data.

2 Data and processing

2.1 Basic data for image simulation

The Moderate Resolution Imaging Spectroradiometer (MODIS) aboard the Terra and Aqua satellites provides complete global data coverage every one to two days at spatial resolutions of 250, 500, and 1000 m, and acquires data in 36 spectral bands between 0.4 μm and 14 μm. Given that MODIS has data gaps on a daily basis, the products, including land surface temperature (LST) and sea surface temperature (SST) from MODIS, and surface temperature retrieved from the microwave brightness temperatures between January 1 and 10, 2005, were selected as the basic data for image simulation. The microwave temperature data retrieved through a statistical scheme (Alsweiss et al., 2017) were used to fill the missing data gaps of MODIS. The global temperature data obtained by fusion of the three types of data were used to simulate the Moon-based microwave brightness temperature images.

2.2 Validation data

The L2A brightness temperature products from the multi-channel Advanced Microwave Scanning Radiometer (AMSR-E) on January 1, 2005 were used to validate the simulation results for the Moon-based microwave radiation brightness temperatures. The AMSR-E aboard the Aqua satellite, launched by the National Aeronautics and Space Administration (NASA) on May 2, 2002, features dual-polarized microwave measurement at frequencies of 6.9, 10.7, 18.7, 23.8, 36.5 and 89 GHz. The geometric correction, image fusion, mosaic and color adjustment were conducted for the AMSR-E data, and the global brightness temperature images with frequencies of 6.9, 10.7, 18.7, 23.8, 36.5 and 89 GHz were generated. Using the brightness temperature data from AMSR-E, the accuracy for the simulation data of the Moon-based microwave radiation brightness temperatures was validated for selected study sites.

3 Methods

Based on the characteristics of a Moon-based Earth observation platform, various factors that influence the Moon-based microwave radiation image simulation (e.g., time zone correction, relative movement of the Earth-Moon, atmospheric radiative transfer and the effect of the ionosphere) were analyzed in this study.

3.1 Time zone correction

Theoretically, each image acquired at the same time (Coordinated Universal Time: UTC) by a Moon-based

platform can cover almost half of the Earth's surface, spanning 12 time zones. However, most of the satellites orbiting the Earth acquire data of its surface with limited coverage and at different times. Although image fusion and mosaic can expand the coverage, the results do not meet the requirements for spatial and temporal consistency due to the different acquisition times. Hence the temperature data, for example, used for image simulation must be corrected to the same UTC. That is, time zone correction of the data must be implemented.

In this study, the diurnal temperature cycle model was used for time zone correction. Due to the variance in diurnal temperature has different characteristics in land and sea surfaces, the time zone corrections were carried out separately. For the SST, the diurnal cycle is related to latitude, season, wind speed, etc., with season as the primary factor. The greatest changes occurred in summer, steadily decreasing in spring, then autumn, with the least change observed in winter. The greatest variance in summertime SST is approximately 0–3 K (Gentemann, 2003; Wang and Zhang, 2017; Yang et al., 2017; Carella et al., 2018). Thus, time zone correction is not necessary due to the minimal effect on the brightness temperatures. However, due to the large temperature variation in the LST, with potential effects on brightness temperatures, the JNG06 diurnal temperature cycle model (Duan et al., 2014, 2012; Schädlich et al., 2001) was used for the LST time zone correction. The model can be written as:

$$T_{\text{day}}(t) = T_0 + T_a\cos[\beta(t-t_m)],\ t < t_s,$$

$$T_{\text{night}}(t) = b_1 + b_2 e^{a(t-t_s)},\ t \geqslant t_s, \tag{1}$$

with

$$b_2 = [-\beta T_a \sin\left(\beta(t_s-t_m)\right)]/\alpha,$$

$$b_1 = T_0 + T_a\cos[\beta(t_s-t_m)] - b_2, \tag{2}$$

where t is the local time, T_0 is the residual temperature around sunrise, T_a is the variation of the LST over a diurnal cycle, t_s is the starting time of the free attenuation, t_m is the time at which the temperature reaches its maximum, and T_0, T_a, t_s, t_m, α, and β are parameters that need to be determined.

As mentioned above, the MODIS carried by the Terra and Aqua satellites can register up to four observations each day at a specific location. There are six free parameters in the above model, all of which must be optimized. Based on a previous study (Duan et al., 2012), the values of t_s and t_m were usually set as 16.5 h and 13.1 h, respectively. The other four free parameters were then determined via four observations. From Eq. (1), ΔT_s from t_1 to t_2 can be expressed as:

$$\Delta T_s = T(t_1) - T(t_2), \tag{3}$$

then,

$$T_s(t_2) = T_s(t_1) + \Delta T_s. \tag{4}$$

3.2 Relative movement of the Earth-Moon

The distance between the Earth and the Moon is about 380000 km. The Moon orbits the Earth in an elliptical orbit with the orbital plane close to the ecliptic plane. Meanwhile, the rotation and revolution of the Moon are synchronous with a period of 27.32 days. Hence, the Moon always faces the Earth allowing for placement of Moon-based sensors on the near side for Earth observation. Moreover, due to the movement of the Earth and the Moon, their relative position constantly varies, resulting in changes of the nadir position and the Moon-based observation area. Figure 1 is a simplified diagram of the relative positions of the Earth and the Moon, where EF is the Earth's rotation axis, point O is the Earth's core, point B is the centroid of the lunar path, point A is a position on the Earth's surface, and H is the projection of A on the ecliptic. The crossing point between OB and the Earth's surface is the nadir (point D). The angle of incidence of microwave radiation can be obtained based on the geometric relationship.

In this study, the JPL ephemeris data were used to obtain the nadir position for Moon-based observation at any time. The solar elevation angle of the Earth's surface from a Moon-based perspective can then be obtained based on parameters such as date, time, latitude, longitude, elevation, and the Earth's curvature. The coverage of Moon-based Earth observations can also be obtained when the solar elevation angle is greater than zero. The calculation of the solar elevation angle can be expressed as:

$$h_c = \arcsin(\sin\delta\sin\varphi + \cos\delta\cos\varphi\cos\tau) + \Delta h_c, \tag{5}$$

where h_c is the solar elevation angle, δ is solar declination, φ is the geographic latitude, τ is the solar hour angle and Δh_c is the angular deflection caused by the specified site elevation. Due to the small change in the solar declination value, the declination angle δ on any day of the year can be expressed as:

$$\begin{aligned}\delta = {} & 0.3723 + 23.2567\sin\theta \\ & + 0.1149\sin2\theta - 0.1712\sin3\theta - 0.758\cos\theta \\ & + 0.3656\cos2\theta + 0.0201\cos3\theta,\end{aligned} \tag{6}$$

with $\theta = 2\pi(N-N_0)/365.2422$, and where N is the number of the date with accumulation starting from January 1 of each year and $N_0 = 79.6764 + 0.2422\times(\text{year}-1985) - int[(\text{year}-1985)/4]$.

As an astronomical parameter, the solar hour angle is defined as the difference between the right ascension of the celestial body and local sidereal time. The formula is

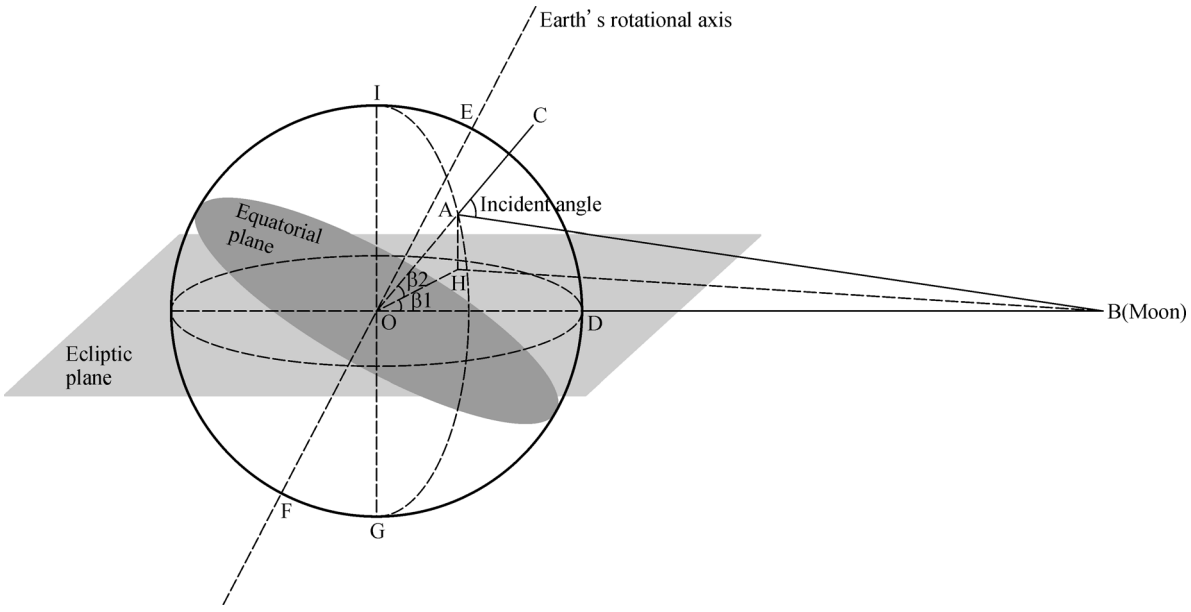

Fig. 1 The relative position between the Earth and the Moon.

expressed as:

$$\tau = S_0 + T - \Delta T - \alpha, \tag{7}$$

where S_0 is the sidereal time at 0 o'clock UTC ($S_0 = 6^h40^m + d \cdot 3^m56^s$, where 6^h40^m is the sidereal time at midnight on New Year's Day and d is the number of the date with accumulation starting from New Year's Day), T is local time, ΔT is the difference between the local geographic longitude and the longitude of the time zone centerline with the units of hour, minute and second, and α is the right ascension.

Finally, according to the relationship between the solar altitude angle and the zenith angle, the zenith angle for Moon-based imaging coverage can be obtained, which can be used as an input parameter for Moon-based microwave radiation image simulation.

3.3 Atmospheric radiative transfer for Moon-based observation

The atmosphere begins at the Earth's surface and extends upward approximately 100 km. The microwave radiation emitted by the Earth's surface would pass through the atmosphere before being received by a Moon-based Earth observation platform. During the actual process of atmospheric transmission, part of the microwave energy would be lost due to absorption and scattering of the radiant energy by the atmosphere. However, radiation emitted from the atmosphere would lead to an increase in the total energy received by the observation platform. The atmospheric parameters for spaceborne microwave radiation imaging may be regarded as being uniform in nature due to the limited coverage and the small viewing zenith angle. However, in the case of an image acquired by a Moon-based observation platform, the coverage would equate to about half of the Earth's surface. In addition, given the wide range of the viewing zenith angle, the atmospheric contribution should be considered due to the atmospheric parameters for Moon-based microwave imaging.

In the context of atmospheric radiation transmission theory, the radiant energy received by a Moon-based microwave radiometer would be made up of four components: 1) microwave radiation of the Earth's surface attenuated by the atmosphere; 2) atmospheric downward radiation reflected by the Earth's surface which is subsequently attenuated by the atmosphere; 3) atmospheric upward radiation; 4) radiation from the sun which is attenuated by the atmosphere (Tatnall et al., 1996; Yujiri et al., 1999; Huang et al., 2001; Yujiri et al., 2003; Zhang et al., 2003; Salmon, 2004 and 2018; Zhang and Wu, 2007). The radiant energy can be expressed as:

$$\begin{aligned} T_{AP}{}'(\theta) = {} & \varepsilon_{\mathrm{p,\,scene}} \cdot T_s \cdot \tau_f(\theta) + T_{\mathrm{atm}\uparrow}(\theta) \\ & + (1-\varepsilon_{\mathrm{p,\,scene}}) \cdot T_{\mathrm{atm}\downarrow}(\theta) \cdot \tau_f(\theta) \\ & + (1-\varepsilon_{\mathrm{p,\,scene}}) \cdot \tau_f^2(\theta) \cdot T_{\mathrm{solar}}, \end{aligned} \tag{8}$$

and

$$T_{\mathrm{atm}\uparrow}(\theta) = \int_0^s k_a(z) T_a(z) e^{-\sec\theta \cdot \int_z^s k_a(z')\mathrm{d}z'} \cdot \sec\theta \mathrm{d}z,$$

$$T_{\mathrm{atm}\downarrow}(\theta) = \sec\theta \int_0^s k_a(z) T_a(z) e^{-\sec\theta \cdot \int_0^z k_a(z')\mathrm{d}z'} \cdot \mathrm{d}z,$$

$$\tau_f(\theta) = \exp\left(-\int_0^s k_a(z)\cdot\sec\theta \mathrm{d}z\right), \quad (9)$$

where $T_{AP}^{'}(\theta)$ is the radiant energy through the atmosphere, $\varepsilon_{p,\mathrm{scene}}$ is the surface microwave emissivity, T_s is the surface temperature, $\tau_f(\theta)$ is the atmospheric transmittance, $T_{\mathrm{atm}\downarrow}(\theta)$ is the atmospheric downward radiation, $T_{\mathrm{atm}\uparrow}(\theta)$ is the atmospheric upward radiation, T_{solar} is the radiation from the sun, K_a is the atmospheric attenuation, $T_a(z)$ is the air temperature, z is the altitude, s is the distance between the antenna of a Moon-based microwave radiometer and the target, and θ is the viewing zenith angle.

Surface microwave emissivity is the key parameter for determining the brightness temperature of objects and depends on surface parameters, such as dielectric constant, surface roughness, temperature, and water content. The surface emissivity of a small area may be estimated based on these surface parameters. However, the surface emissivity of a large area for Moon-based observation would need to be calculated by the radiative transfer equation due to the low resolution of the microwave radiometer and the effect of mixed pixels. The formula for surface microwave emissivity is given in Eq. (10):

$$\varepsilon_p = \frac{T_{\mathrm{BT}} - T_{\mathrm{atm}\uparrow} - T_{\mathrm{atm}\downarrow}\cdot\gamma}{\gamma\cdot(T_0 - T_{\mathrm{atm}\downarrow})}, \quad (10)$$

where T_{BT} is the microwave radiation brightness temperature, T_0 is the surface temperature, $T_{\mathrm{atm}\uparrow}$ is the atmospheric upward radiation, $T_{\mathrm{atm}\downarrow}$ is the atmospheric downward radiation, and γ is the atmospheric transmittance. In this study, the surface microwave emissivity was obtained using the microwave brightness temperatures, the land surface temperatures, and the atmospheric profile data.

Atmospheric attenuation is another factor that would influence Moon-based Earth observations and is related to the absorption and scattering by particles and molecules in the atmosphere, including aerosols, water vapor, carbon dioxide, and oxygen. In the microwave and millimeter wave bands, absorption by oxygen and water vapor is the main factor that influences atmospheric attenuation. Based on the International Telecommunication Union Radio communication sector (ITU-R) P Series P.676-8 recommendation, an estimation of the atmospheric attenuation of microwaves (0–1000 GHz) can be obtained by the line-by-line method. The method adopts a way of accumulating the respective resonance lines of oxygen and water vapor to enable calculation of the atmospheric attenuation of radio waves at any pressure, temperature, or humidity. For an air pressure of 1013 hPa, a temperature of 15°C, and a water vapor density of 7.5 g/m^3 (wet conditions, water vapor), and 0 g/m^3 (dry conditions, oxygen), the atmospheric attenuation due to oxygen and water vapor in the 0–1000 GHz region is illustrated in Fig. 2(a). There are multiple water vapor absorption bands in the 0–1000 GHz region and eight absorption lines for oxygen. Moreover, from the theoretical expressions for atmospheric transmittance, the atmospheric transmittance is closely related to atmospheric attenuation at the different heights. Figure 2(b) shows the

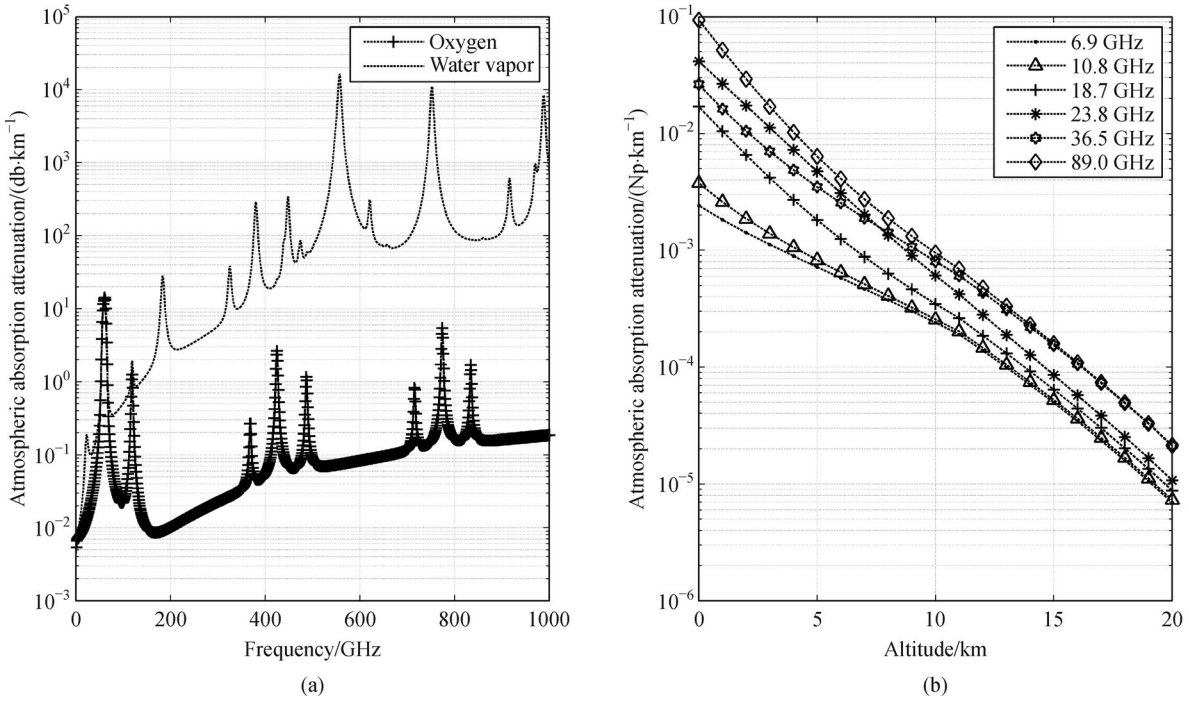

Fig. 2 (a) Atmospheric attenuation caused by oxygen and water vapor at 0–1000 GHz. (b) The change of atmospheric attenuation with altitude at different frequencies.

variation in atmospheric attenuation with altitude at different microwave frequencies. As the altitude increases, the atmospheric attenuation gradually decreases. When the altitude is higher than 10 km, the atmospheric attenuation is near zero.

In this study, the vertical atmosphere was divided into 20 layers and the atmospheric radiation of each layer, which would influence the Moon-based observation, can be calculated. Input parameters for this model included meteorological factors, such as pressure, temperature, humidity, and variable gas concentrations derived from numerical weather prediction models, as well as surface temperature, surface emissivity, and the zenith angle. First, given the initial variables for the model, the atmospheric attenuation and transmittance of each layer were obtained. The Moon-based microwave radiation of each layer was then calculated based on these known parameters using Eqs. (8) and (9). Finally, the total microwave radiation observed by the Moon-based microwave radiometer was obtained.

3.4 The effect of the ionosphere

The ionosphere, an important element of the Earth-space environment, exists in the upper atmosphere and extends between 90 km to 1000 km from the Earth's surface. The medium consists of many free electrons and ions formed as a result of interactions with solar radiation. The electron concentration of the ionosphere varies significantly at different heights. Due to the limited orbital height of a low-orbit satellite platform, the effect of the ionosphere on spaceborne microwave imaging usually does not need to be considered. However, a Moon-based platform located outside the Earth's ionosphere can result in a change in the propagation path of the microwave radiation and can attenuate the microwave signal as a consequence of the collisions between electrons, ions, and neutral particles. The attenuation is closely related to the microwave frequency, the collision frequency of the electrons, and the vertical profile of the electron density (Laroussi and Roth, 1993; Devi et al., 2008; Cong et al., 2018). Thus, the effect of the ionosphere on Moon-based observations at different microwave frequencies needs to be examined in detail.

As shown in Eq. (11), an empirical model for the vertical distribution of the electron concentration of the ionosphere has been used to describe the distribution of the ionospheric electron concentration (Yu, 2012). In Eq. (11), N_mE is the maximum electron concentration of layer E, h_mE is the corresponding height of layer E, y_mE is the half layer thickness of E, y_mF_2 is the half layer thickness of F_2, h_j is the height of the ionosphere when the electron concentration is N_j, the electron concentration N_j is a linear distribution when the height is lower than h_j, N_j is a parabolic distribution when the height is larger than h_j, and $H = 1.66[30 + 0.075(h_mF_2 - 200)]$.

$$N_e = \begin{cases} N_mE\left[1-\left(\dfrac{h-h_mE}{y_mE}\right)^2\right] & h_mE - y_mE \leqslant h \leqslant h_mE \\ \dfrac{N_j - N_mE}{h_j - h_mE}h + \dfrac{N_mE\cdot h_j - N_j\cdot h_mE}{h_j\cdot h_mE} & h_mE < h \leqslant h_j \\ N_mF_2\left[1-\left(\dfrac{h-h_mF_2}{y_mE}\right)^2\right] & h_j < h \leqslant h_mF_2 \\ N_mF_2\exp\left[\dfrac{1}{2}\left(1-\dfrac{h-h_mF_2}{H}-e^{-\frac{h-h_mF_2}{H}}\right)\right] & \\ & h_mF_2 < h \leqslant 1000 \text{ km}. \end{cases} \tag{11}$$

The propagation of microwave radiation through the ionosphere is dependent on the variation of the ionospheric refractive index, which in turn is correlated positively with the electron concentration at the corresponding propagation layer. The atmospheric refractive index can be expressed as Eq. (12). Moreover, the ionospheric attenuation varies greatly at different heights due to the change of electron concentration. The attenuation coefficient at different altitudes can be expressed by Eq. (13):

$$n = \sqrt{1-\frac{\omega_p^2}{\omega^2}} = \sqrt{1-\frac{N_e e^2}{4\pi^2\varepsilon_0 m f^2}}, \tag{12}$$

$$\alpha = \frac{\omega}{\sqrt{2}c}\cdot\left(\sqrt{\left(1-\frac{\omega_p^2}{\omega^2+V_m^2}\right)^2+\left(\frac{V_m}{\omega}\cdot\frac{\omega_p^2}{\omega^2+V_m^2}\right)^2} - \left(1-\frac{\omega_p^2}{\omega^2+V_m^2}\right)\right)^{1/2}, \tag{13}$$

where ω is the microwave angular frequency, V_m is the collision frequency of the plasma, ω_p is the plasma frequency, e is the elementary charge, m is the electron mass, ε_0 is the vacuum permittivity, and N_e is the electron concentration. The total attenuation of the microwave radiation in the ionosphere can be obtained by integrating the attenuation coefficient at different altitudes along the entire propagation path of the microwave radiation in the ionosphere, expressed as Eq. (14),

$$Att(db) = 8.68\int_s a\mathrm{d}S, \tag{14}$$

where S is the propagation path for microwave radiation in the ionosphere.

4 Results and discussion

4.1 Analysis of the various factors

1) Time zone correction

The globe was divided into 36 regions based on the time zone and latitude, and the diurnal temperature cycle model of the LST for each region was constructed using the parameters shown in Table 1. Then, based on the diurnal temperature cycle model, the LST obtained at different times (13:30 local time) was normalized to the temperature at the same UTC. When the temperature was normalized to 12:00 (UTC) on January 1, 2005, each time zone from west to east corresponded to 00:00 to 24:00 local time, and the LST obtained at 13:30 local time was normalized to the temperature from 00:00 to 24:00 local time, respectively. Figures 3 and 4 show the distributions of global LST before and after time zone correction. It can be seen that the temperature variation decreased gradually from west to east followed by a gradual increase.

In addition, a comparison of the LST after time zone correction and the MODIS LST product was conducted to validate the accuracy of time zone correction (Fig. 5). The black dots correspond to the LST data from MODIS at four different times (10:30, 13:30, 22:30, and 1:30, local time), and the black line represents the fitting results for LST after time zone correction. Figure 5 shows that the two LSTs are similar and the error is always less than 5 K at the different study sites, indicating that the time zone correction is reliable.

2) Relative movement of the Earth-Moon

In this study, we analyzed the coverage of Moon-based imaging and the zenith angle distribution at different times. Figure 6 shows the nadir position, the coverage of Moon-based imaging, and the zenith angle distribution at UTC 04:00, 08:00, 12:00, 16:00, 20:00, and 24:00, respectively, on January 1, 2005. The results show that the zenith angle of the coverage for Moon-based Earth observation ranges from 0° to 90° and the nadir is located in the position with a zenith angle of 0°. The image acquired by a Moon-based Earth observation platform can cover almost half of the Earth's surface at different times, but the imaging position changes with the relative movement of the Earth and the Moon. Given that the angular velocity of the Earth's rotation is much larger than the angular velocity of the Moon's revolution, the Moon moves from east to west from the perspective of the Earth. As shown in Fig. 6, the nadir position moves from east to west from 04:00 to 24:00, consistent with the relative movement of the Earth and the Moon, indicating that the imaging position of the Moon-based Earth observation also changes. In addition, the imaging position of the Moon-based Earth observation at UTC 04:00 on January 1, 2005 (UTC) is obtained. As the imaging position changes from east to west over time, the Moon-based platform can observe the entire Earth by about UTC 16:00. Also, from 08:00 to 20:00 and also from 12:00 to 24:00, the Moon-based observation can almost cover the whole of the Earth's surface. Hence, it takes about 12 h for the Moon-based platform to acquire complete observation of the Earth.

3) The effect of the atmosphere

The effect of the atmosphere on Moon-based observa-

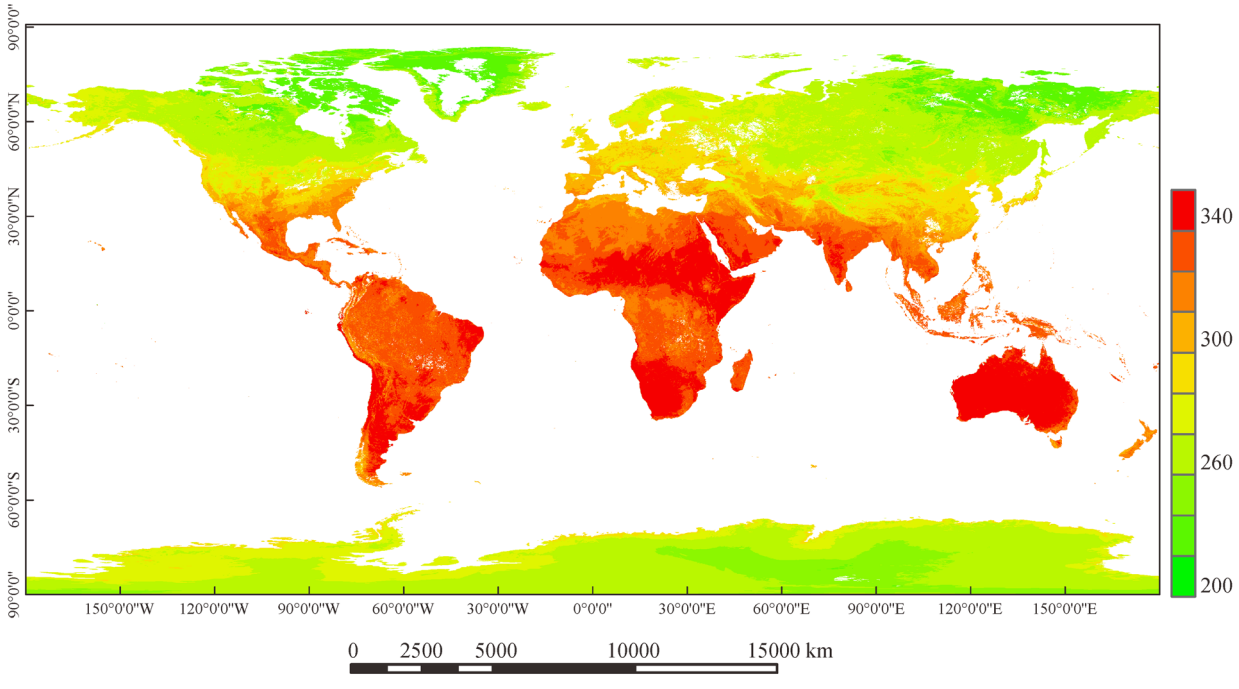

Fig. 3 Distribution of global LST before time zone correction.

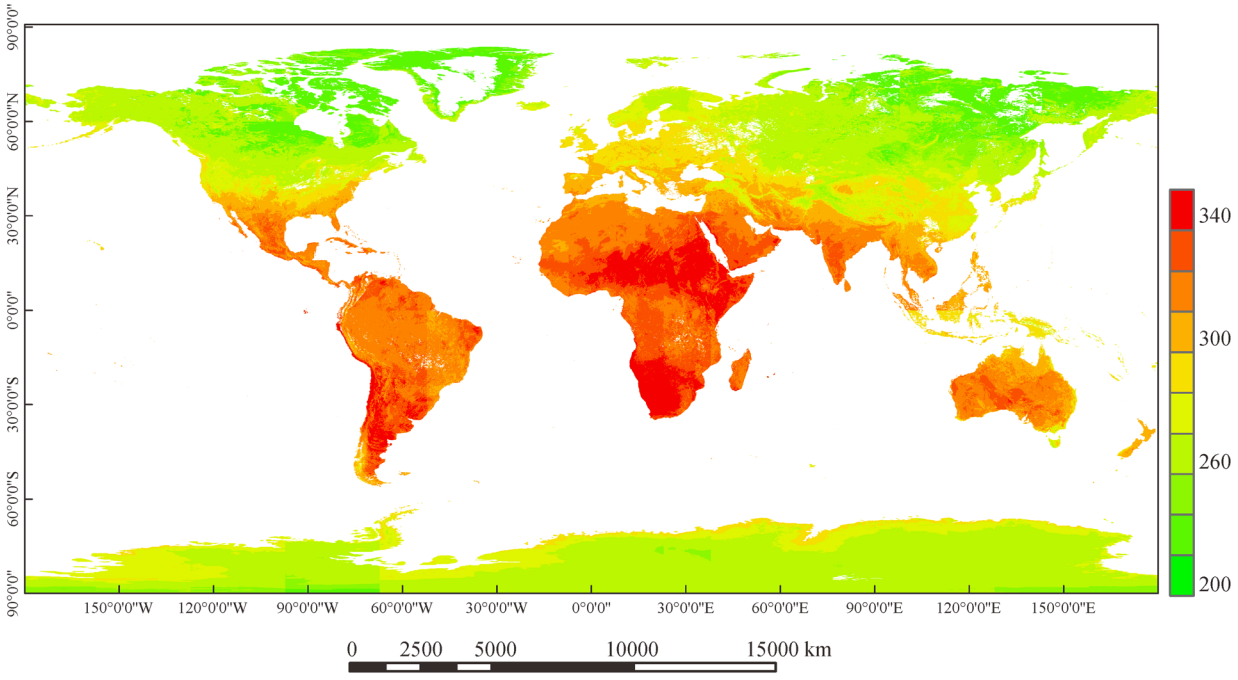

Fig. 4 Distribution of global LST after time zone correction.

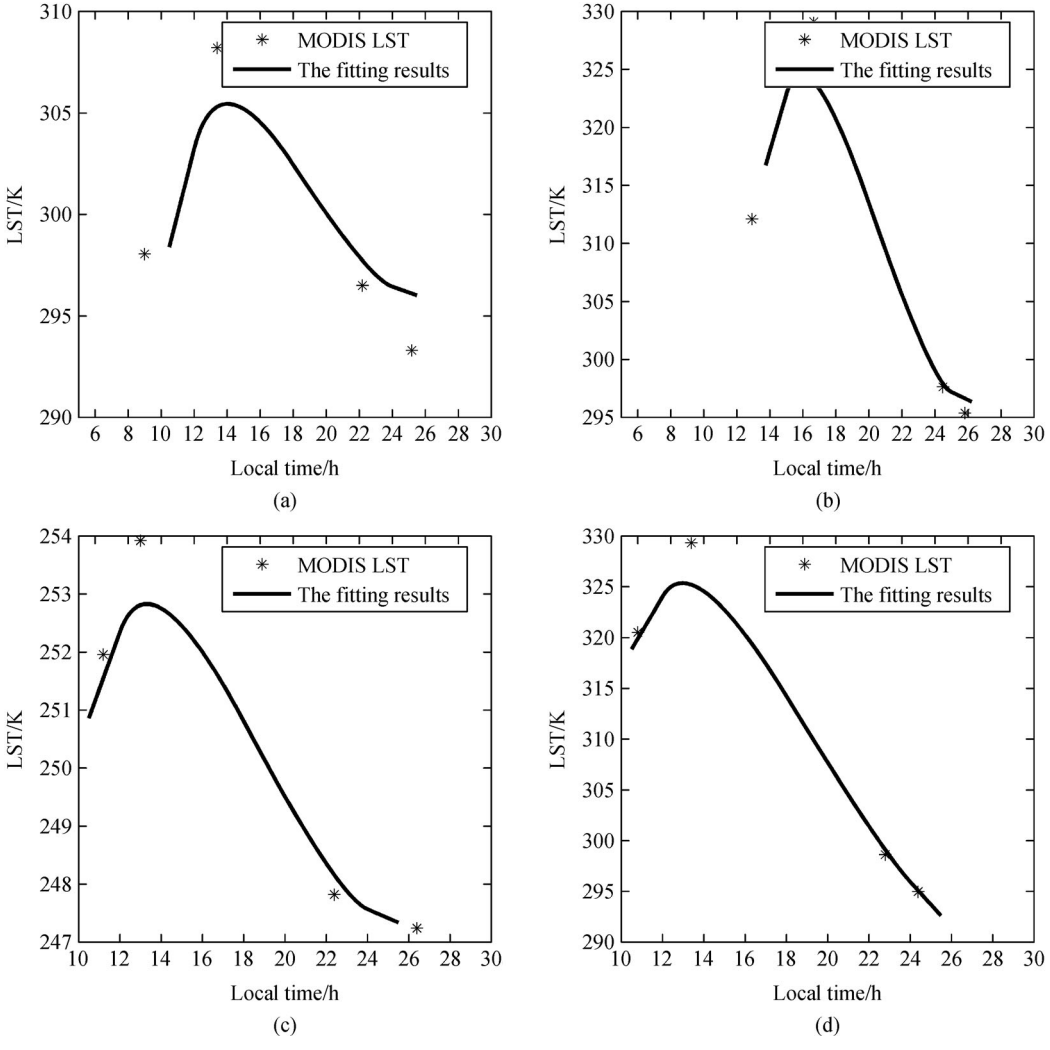

Fig. 5 The fitting results of the LST and MODIS LST data for the four MODIS pixels. (a) South America (b) Oceania (c) Asia and Europe (d) Africa.

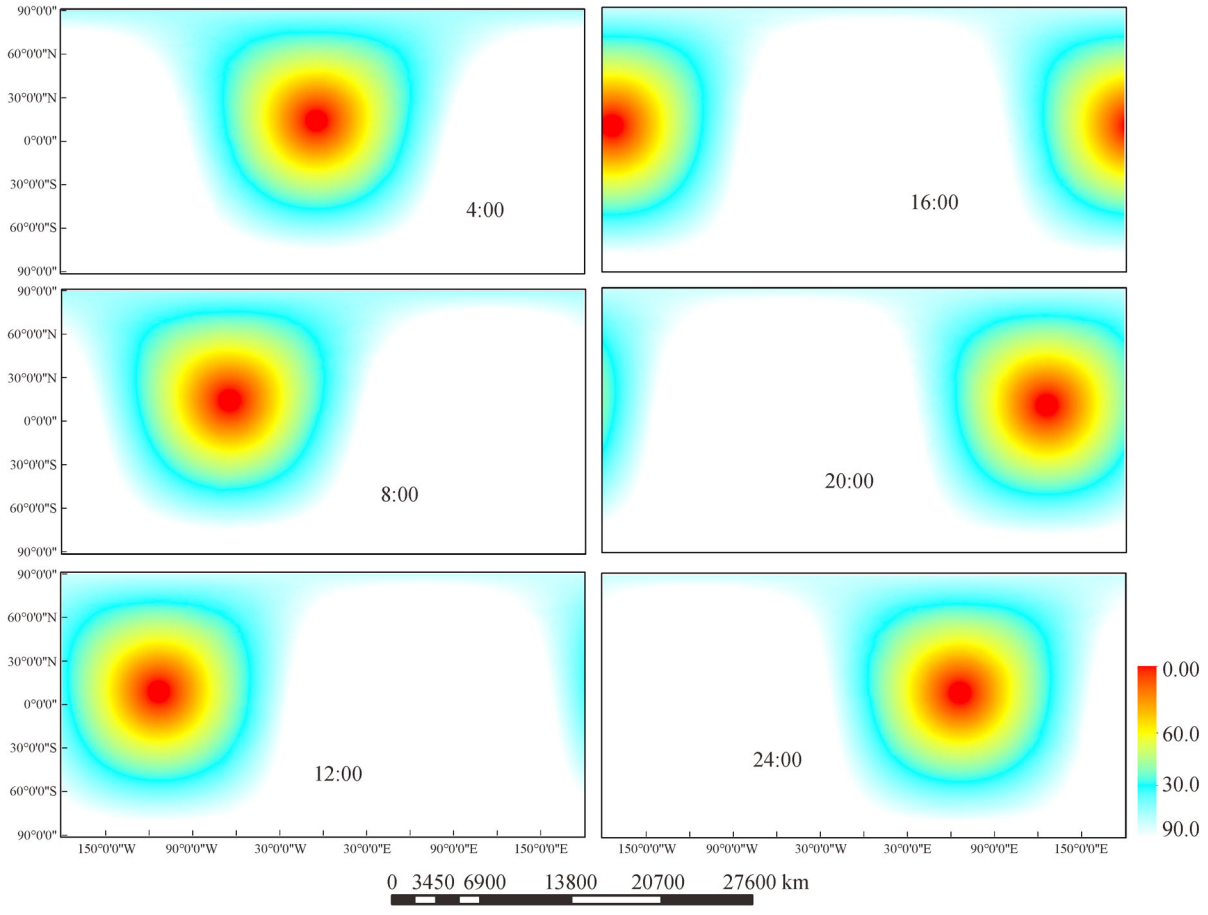

Fig. 6 The Moon-based imaging coverage and zenith angle distribution at different times on January 1, 2005.

tion is dependent on atmospheric pressure, temperature, humidity, water vapor, carbon dioxide, oxygen, viewing zenith angle, and microwave frequency. These factors can significantly affect the atmospheric transmittance and the upward and downward radiation, etc. Figure 7 shows the change of atmospheric transmittance and upward radiation with atmospheric humidity, temperature, viewing zenith angle and microwave frequency. As the atmospheric humidity and temperature increase, the atmospheric transmittance also increases. However, the atmospheric upward radiation decreases with increase of atmospheric humidity and temperature, and there is a positive correlation between atmospheric upward radiation and atmospheric temperature at a frequency of 23.8 GHz (Figs. 7(a)–(d)). With the increase of the viewing zenith angle, the atmospheric transmittance decreases and atmospheric upward radiation increases. These parameters have a higher and a lower growth rate, respectively, with an increase of the viewing zenith angle (Figs. 7(e) and 7(f)). There is a nonlinear relationship between frequency and atmospheric transmittance as well as for upward radiation (Figs. 7(g) and 7(h)). When the frequency is about 25 GHz and 60 GHz, the atmospheric transmittance has a much lower value, and the atmospheric upward radiation reaches a high value.

4) Effect of the ionosphere

The effect of the ionosphere on microwave transmission was analyzed from several aspects, such as collision frequency, microwave frequency, and angle of incidence. Figure 8(a) shows the relationship between the attenuation of microwave energy and collision frequency for microwave transmission in the ionosphere. When the collision frequency is from 1 MHz to 1000 MHz, the attenuation slowly increases, and the low-frequency microwave radiation has a higher growth rate than the high-frequency microwave radiation with increase of collision frequency. Figure 8(b) shows the change in attenuation with microwave frequency in the ionosphere at different angles of incidence. As the frequency increases, the attenuation of the microwave energy in the ionosphere slowly decreases; when the frequency is constant, the attenuation of the microwave energy increases with increase in angle of incidence. Figure 9 shows a comparison of the simulated brightness temperatures which are, and are not, influenced by the ionosphere. The results indicate that the ionosphere has a large effect on the brightness temperatures at low

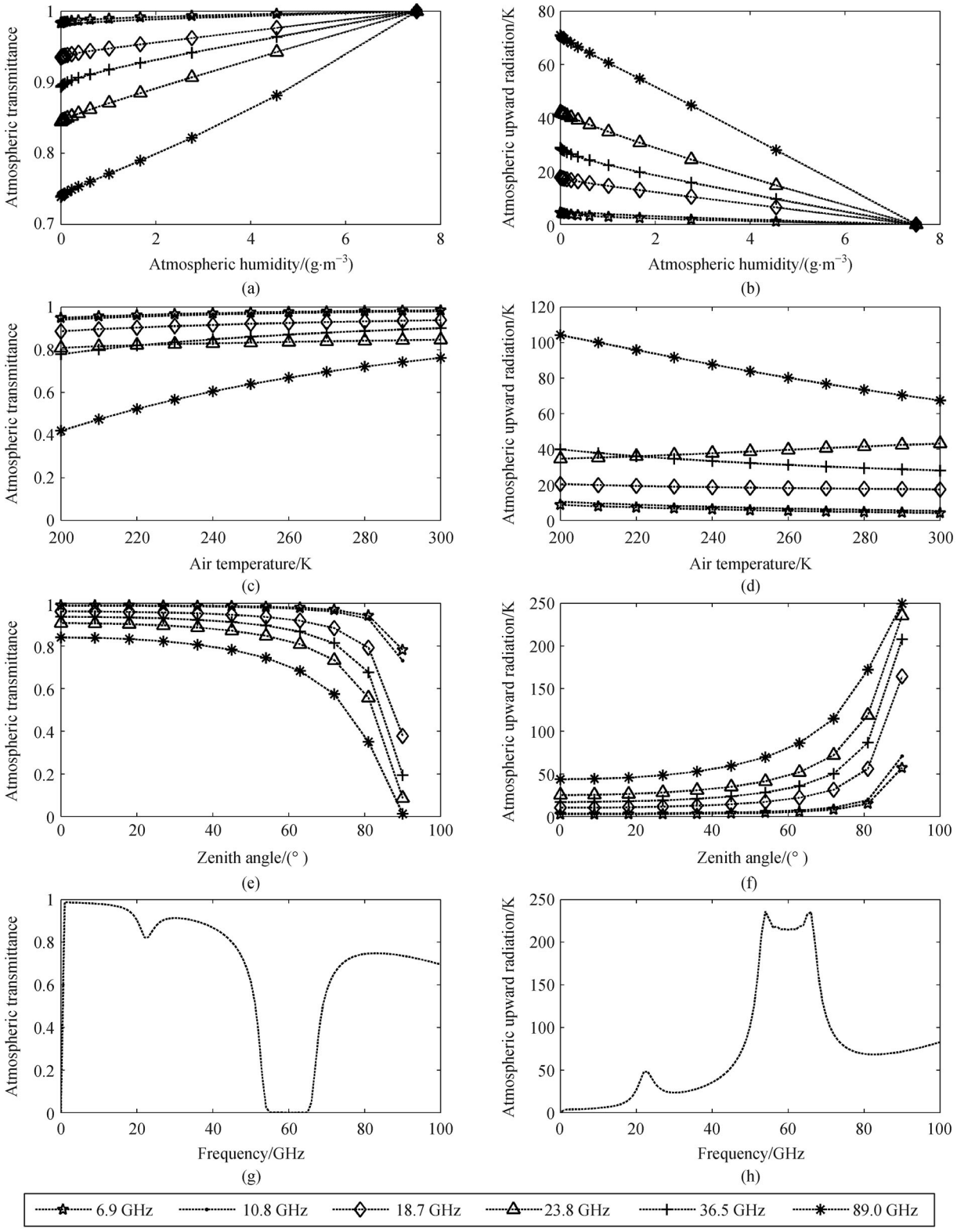

Fig. 7 The change of atmospheric transmittance and upward radiation with atmospheric humidity, temperature, viewing zenith angle, and frequency.

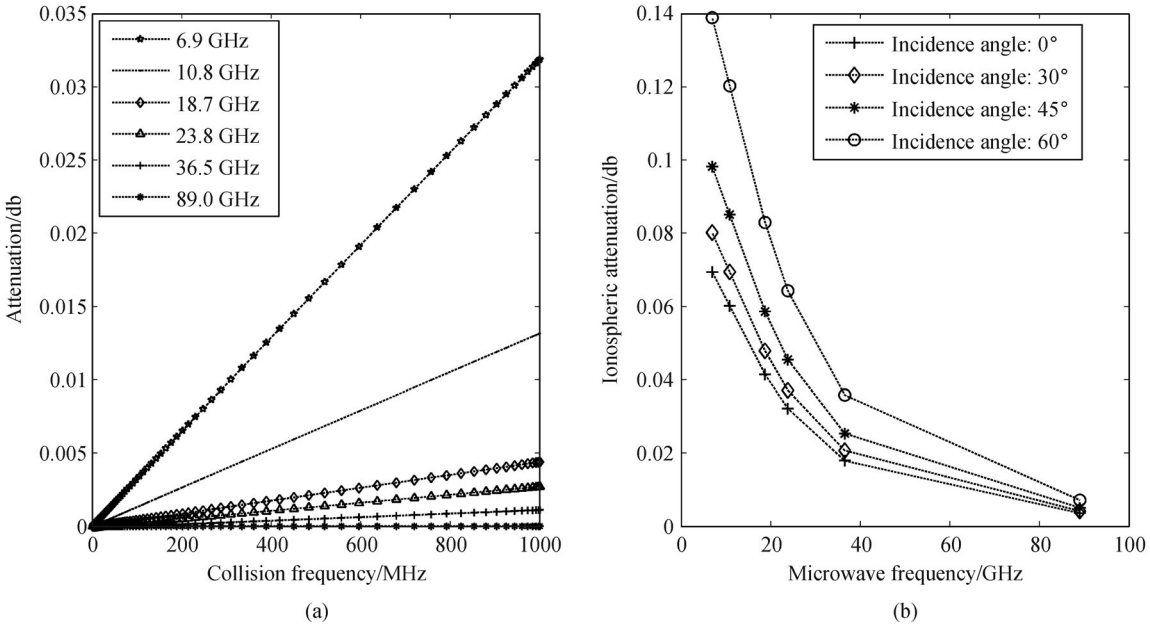

Fig. 8 (a) The change in attenuation of microwave energy with collision frequency in the ionosphere. (b) The change of attenuation of microwave energy with microwave frequency in the ionosphere.

frequency and that the effect decreases with increase of frequency. The average values of change for the brightness temperatures were 3.78 K, 2.12 K, 1.33 K, 1.17 K, 1.01 K, and 0.88 K at frequencies of 6.9, 10.7, 18.7, 23.8, 36.5, and 89.0 GHz, respectively.

4.2 Simulation of Moon-based microwave radiation brightness temperatures

In this section, focus is given to Moon-based microwave radiation image simulation. The basic data used for image simulation have a spatial resolution of 5.6 km (0.05 degree), while the simulated data at different frequencies have different spatial resolutions. Given the analysis of spatial resolution requires the design of a Moon-based sensor hardware system, this aspect is not considered in this discussion.

Considering the requirements for a Moon-based Earth observation platform, the antenna aperture for a Moon-based microwave radiometer was set to 22 m, with the simulation results judged as realistic for this aperture size. Consideration was also given as to the influence of various other factors, including time zone correction, relative movement of the Earth-Moon, atmospheric radiative transfer, and the effect of the ionosphere. The Moon-based microwave brightness temperature images based on operating frequencies of 6.9, 10.7, 18.7, 23.8, 36.5, and 89.0 GHz, respectively, at UTC 08:00 and 12:00 on January 1, 2005 were then simulated using the spaceborne temperature data (Figs. 10 and 11). From these figures, it can be seen that the brightness temperatures on the simulated images gradually increase with increase of frequency.

The study areas, located in North America, South America, Africa, Asia, Europe, Oceania and Antarctica were selected for error analysis of the imaging simulations. The brightness temperature data acquired by the AMSR-E microwave radiometer were used to validate the simulated images. Figure 12 reveals the differences of the two brightness temperature data sets for the different study areas. The results show that the Moon-based Earth observation platform acquires lower brightness temperatures than the satellite platform, and the change in brightness temperatures for the land surface is less than that of the sea surface with an increase in frequency. When the frequency is greater than 89.0 GHz, the brightness temperatures for Moon-based observation are similar to the spaceborne observation. Figure 13 shows the root mean square error (RMSE) of the simulation results at the different sites and where the land surface RMSE ranges from 0 K to 2 K. The accuracy is higher in the low latitude area than in the high latitude area.

The comparison of the errors for the LST and the SST is shown in Table 2. Note that the land surface is more complex than the sea surface, hence the diurnal variation in the LST is much higher than that for the SST. The brightness temperatures for the Moon-based simulation on the land surface have larger errors than that for the sea surface. The average error is 6.32 K for the land surface and 2.70 K for the sea surface, while the relative error for land is 3.59% and 1.13% for the sea and the RMSE is 1.72 K for the land and 0.73 K for the sea. These results

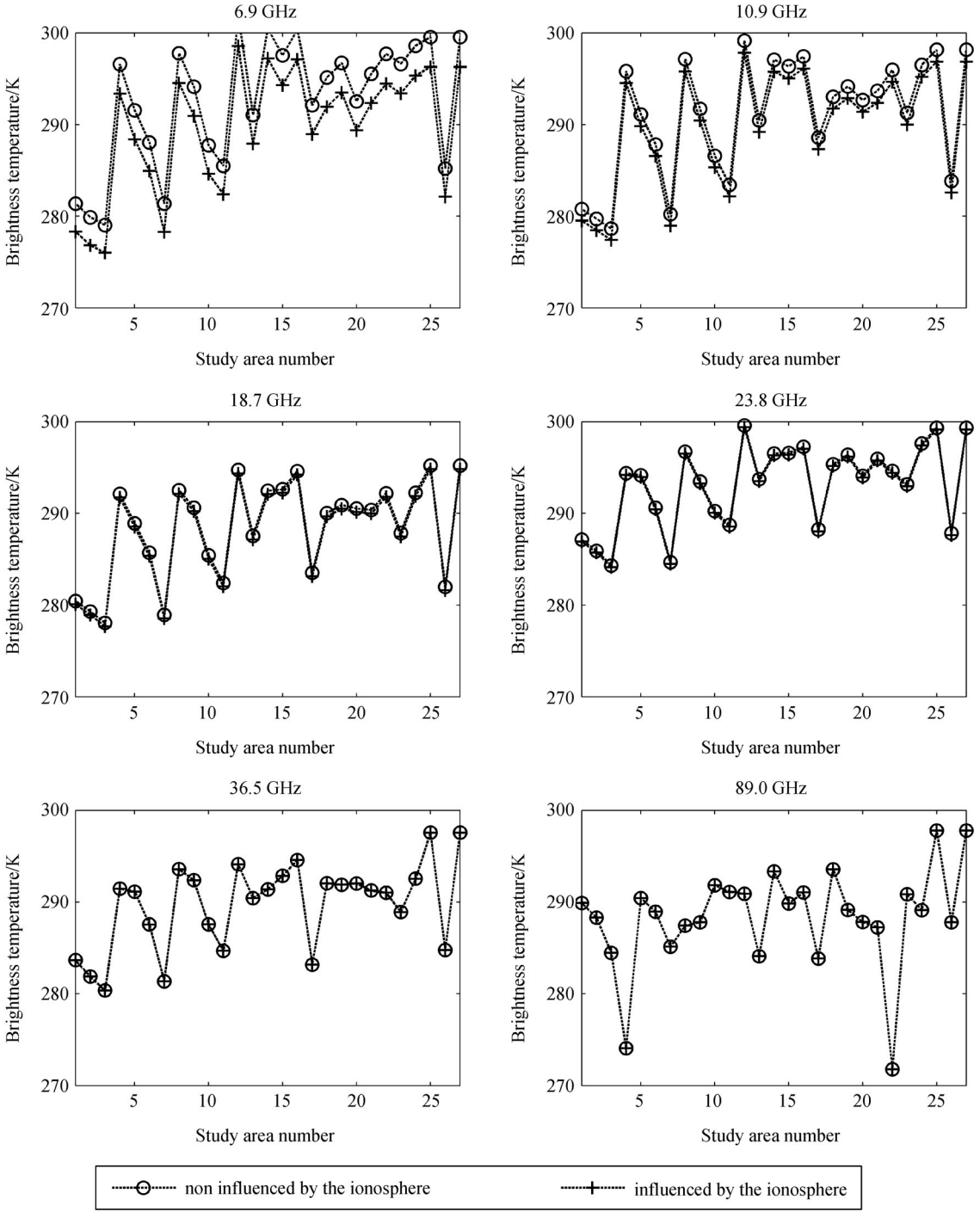

Fig. 9 Comparison of the effect of the ionosphere on Moon-based microwave radiation brightness temperatures at different frequencies.

indicate that the brightness temperatures for Moon-based microwave image simulation are reliable due to the high accuracy of the simulation.

5 Conclusions

Several factors were found to influence the Moon-based microwave radiation image simulation, including the time zone correction, the relative movement of the Earth-Moon, atmospheric radiative transfer, and the effect of the ionosphere. The following conclusions are made. 1) Time zone correction ensures that the images from Moon-based Earth observation may be acquired at the same UTC. The LST may be corrected using the diurnal temperature cycle and the SST does not need to be

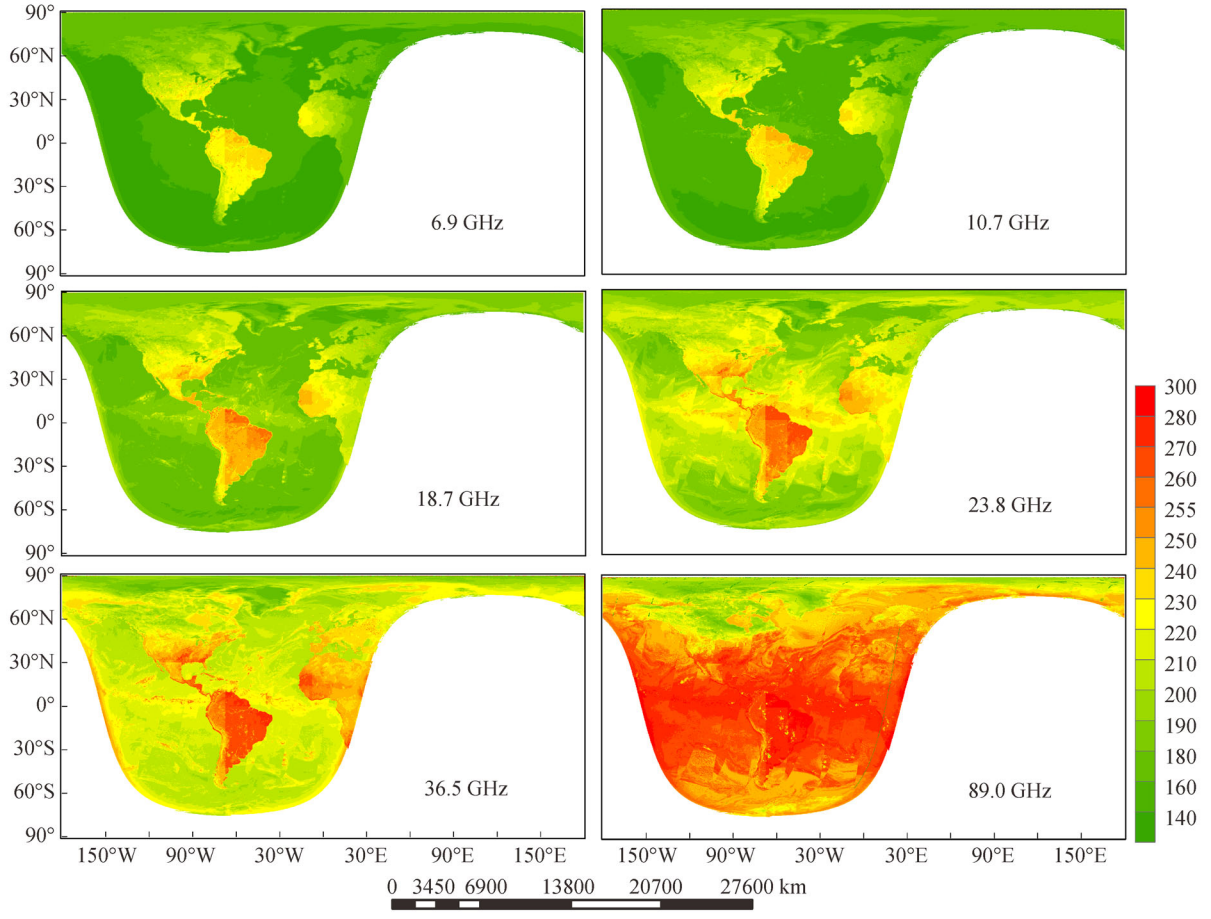

Fig. 10 The images for simulation of the Moon-based microwave radiation brightness temperatures at UTC 08:00 on January 1, 2005.

corrected. 2) The relative movement of the Earth-Moon influences the nadir position and the position for Moon-based imaging. The nadir position moves from east to west over time, consistent with the changes of imaging position for Moon-based Earth observation. The zenith angle of the coverage for Moon-based Earth observation ranges from 0° to 90°, such that the Moon-based platform takes about 12 h to measure a complete observation of the Earth. 3) The atmospheric effects are related to atmospheric pressure, temperature, humidity, water vapor, carbon dioxide, oxygen, viewing zenith angle, and microwave frequency. These factors have an effect on the atmospheric transmittance as well as upward and downward propagation of radiation. With an increase in atmospheric humidity and temperature, and a decrease in the viewing zenith angle, the atmospheric transmittance increases and the atmospheric upward radiation decreases. 4) The ionosphere attenuation is related to collision frequency, microwave frequency, and viewing zenith angle. As the collision frequency increases, the attenuation of microwave energy slowly increases, and the low-frequency microwave radiation has a higher growth rate than the high-frequency microwave radiation with an increase of collision frequency. With the increase in microwave frequency, the attenuation decreases rapidly, but increases with the increase of the viewing zenith angle.

After examination of the various factors, the images for Moon-based microwave brightness temperature were simulated. The brightness temperature data acquired by the AMSR-E microwave radiometer were used to validate the simulated images for the Moon-based microwave radiation brightness temperatures. The results showed that the Moon-based Earth observation platform provided lower brightness temperatures than that of the satellite platform, and the brightness temperatures for the land surface changes were less than that for the sea surface with increase of frequency. Moreover, the RMSE of the simulated data was less than 2 K, indicating that the method used in this study is viable and may be used to simulate images of Moon-based microwave brightness temperatures.

In the context of Moon-based Earth observation, microwave radiation image simulation may be used to support studies aimed at better understanding the features of Moon-based microwave radiation imaging and checking

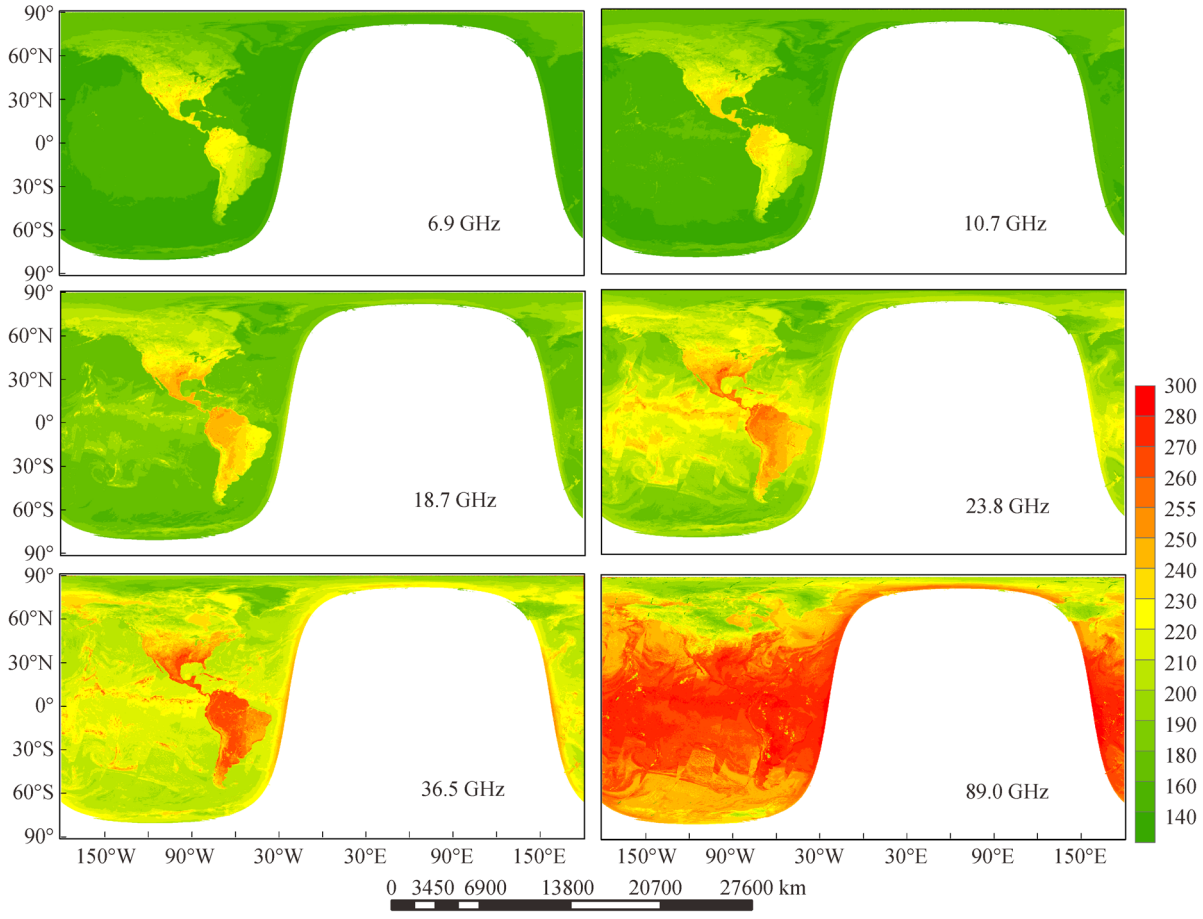

Fig. 11 The images for simulation of the Moon-based microwave radiation brightness temperatures at UTC 12:00 on January 1, 2005.

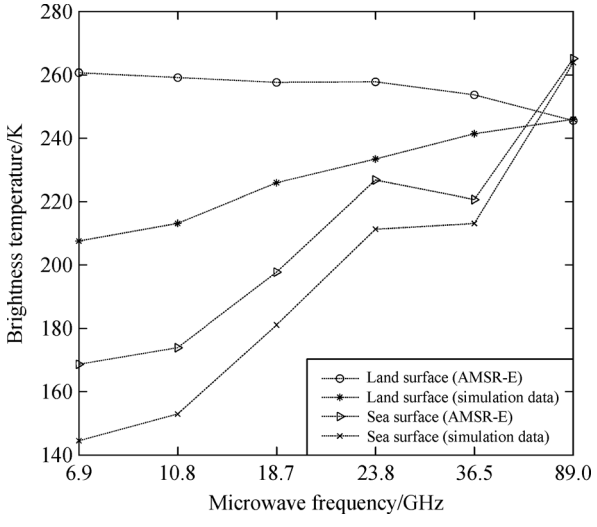

Fig. 12 The comparison of the brightness temperatures for the Moon-based simulation and the AMSR-E microwave radiometer.

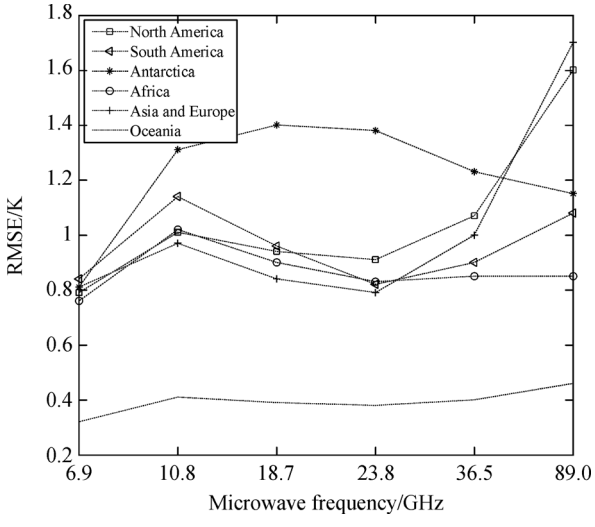

Fig. 13 The root mean square error (RMSE) of the Moon-based simulation images for the different continents.

the quality of the microwave measurements. Moreover, this research may serve as a basis for the Moon-based system design. Future work on microwave radiation image simulation will be directed at devising more efficient methods for image simulation including investigation of other performance parameters.

Acknowledgements This work was supported by the National Natural Science Foundation of China (Grant No. 41590855) and the Key Research Project in Frontier Science of the Chinese Academy of Sciences (No. QYZDY-SSW-DQC026). We are grateful to students and teachers of our research group for providing help and writing assistance. We are also grateful to the National Aeronautics and Space Administration (NASA) and the National Snow and Ice Data Center (NSIDC) for providing MODIS and AMSR-E data. We would like to thank the anonymous reviewers for their voluntary work and the constructive comments which helped to improve the manuscript.

Appendix

Table A1 The fitting results for parameters of the diurnal temperature cycle model

Number	T_0/K	T_a/K	α	β
1	234.647	7.34024	−1.01117	1.0071
2	243.706	5.25396	−5.68419	0.40823
3	286.887	15.0345	−3.12953	0.441291
4	226.487	47.8038	−1.32001	1.20496
5	260.121	6.91076	−1.78134	1.12404
6	256.971	3.16141	−2.92833	1.21333
7	279.69	28.5639	−6.18648	0.454205
8	292.803	10.9054	0.099393	0.277346
9	293.764	9.25083	−0.19969	−0.33375
10	287.412	7.90905	−0.71262	0.365055
11	291.317	12.813	−0.55321	0.39392
12	222.112	24.5167	0.22719	0.965652
13	234.647	7.34024	−1.01117	1.0071

Table A2 Comparison of accuracy for Moon-based microwave radiation image simulation

	Frequency/GHz	6.9 GHz	10.8 GHz	18.7 GHz	23.8 GHz	36.5 GHz	89.0 GHz
Land surface	Average error/K	5.29	6.32	4.96	3.34	3.68	1.36
	RMSE/K	1.10	1.51	1.55	1.52	1.53	1.72
	Relative error	3.11%	3.59%	2.47%	1.45%	1.64%	0.51%
Sea surface	Average error/K	1.02	1.45	1.63	1.61	2.05	2.70
	RMSE/K	0.10	0.18	0.43	0.73	0.50	0.42
	Relative error	0.40%	0.57%	0.65%	0.64%	0.83%	1.13%

References

Alsweiss S O, Jelenak Z, Chang P S (2017). Remote sensing of sea surface temperature using AMSR-2 measurements. IEEE J-STARS, 10(9): 3948–3954

Carella G, Kennedy J, Berry D I, Hirahara S, Merchant C J, Morak-Bozzo S, Kent E C (2018). Estimating sea surface temperature measurement methods using characteristic differences in the diurnal cycle. Geophys Res Lett, 45(1): 363–371

Cong C, Shi C, Shi Z (2018). A comparative study on electromagnetic wave propagation in a plasma sheath based on double parabolic model. Optik (Stuttg), 159: 69–78

Devi M I, Khan I, Rao D N M (2008). A study of VLF wave propagation characteristics in the earth-ionosphere waveguide. Earth Planets Space, 60(7): 737–741

Ding Y, Guo H, Liu G (2014). Potential applications of the moon based synthetic aperture radar for earth observation. IEEE Int Geosci Remote Sens Symp: 1767–1769

Duan S B, Li Z L, Tang B H, Wu H, Tang R (2014). Direct estimation of land-surface diurnal temperature cycle model parameters from MSG-SEVIRI brightness temperatures under clear sky conditions. Remote Sens Environ, 150: 34–43

Duan S B, Li Z L, Wang N, Wu H, Tang B H (2012). Evaluation of six land-surface diurnal temperature cycle models using clear-sky in situ and satellite data. Remote Sens Environ, 124: 15–25

Fornaro G, Franceschetti G, Lombardini F, Mori A, Calamia M (2010). Potentials and limitations of moon-borne SAR imaging. IEEE T Geosci Remote, 48(7): 3009–3019

Gentemann C L (2003). Diurnal signals in satellite sea surface temperature measurements. Geophys Res Lett, 30(3): 1140

Guo H D, Ding Y X, Liu G, Zhang D W, Fu W X, Zhang L (2014). Conceptual study of lunar-based SAR for global change monitoring. Sci China Earth Sci, 57(8): 1771–1779

Guo H D, Liu G, Ding Y X (2018). Moon-based Earth observation: scientific concept and potential applications. Int J Digit Earth, 11(6): 546–557

Guo H, Liu G, Ding Y, Zou Y, Huang S, Jiang L, Gensuo J, Lv M, Ren Y, Ruan Z, Ye H (2016). Moon-based earth observation for large scale geoscience phenomena. IEEE Int Geosci Remote Sens Symp: 546–557

Hamill P (2007). Atmospheric observations from the moon: a lunar earth-observatory. In: NASA advisory council workshop on science associated with the lunar exploration architecture white papers

Huang Q L, Zhang Z Y, Guo W (2001). Approach to generate radiometric images. Int J Infrared Milli, 22(12): 1805–1811

Huang S (2004). Merging information from different resources for new insights into climate change in the past and future. Geophys Res Lett, 31(13)

Huang S (2008). Surface temperatures at the nearside of the moon as a record of the radiation budget of Earth's climate system. Adv Space Res, 41(11): 1853–1860

Johnson J R, Lucey P G, Stone T C, Staid M I (2007). Visible/near-infrared remote sensing of Earth from the moon. In: NASA advisory council workshop on science associated with the lunar exploration architecture white papers

Laroussi M, Roth J R (1993). Numerical calculation of the reflection, absorption, and transmission of microwaves by a nonuniform plasma slab. IEEE Trans Plasma Sci, 21(4): 366–372

Ren Y, Guo H, Liu G, Ye H (2017). Simulation study of geometric characteristics and coverage for Moon-based earth observation in the electro-optical region. IEEE J STARS, 10(6): 2431–2440

Salmon N A (2004). Polarimetric scene simulation in millimeter-wave radiometric imaging. Proc SPIE Int Soc Opt Eng, 5410(7): 260–269

Salmon N A (2018). Outdoor passive millimeter wave imaging: phenomenology and scene simulation. IEEE Trans Antenn Propag, 66(2): 897–908

Schädlich S, Göttsche F M, Olesen F S (2001). Influence of land surface parameters and atmosphere on METEOSAT brightness temperatures and generation of LST maps by temporally and spatially interpolating atmospheric correction. Remote Sens Environ, 75(1): 39–46

Tatnall A R L, Donnelly R P, Charlton J E C (1996). Microwave radiometer model simulation. Int J Remote Sens, 17(16): 3107–3120

Wang X H, Zhang H (2017). Effects of Australian summer monsoon on sea surface temperature diurnal variation over the Australian north-western shelf. Geophys Res Lett, 44(19): 9856–9864

Yang X, Song Z, Tseng Y H, Qiao F, Shu Q (2017). Evaluation of three temperature profiles of a sublayer scheme to simulate SST diurnal cycle in a global ocean general circulation model. J Adv Model Earth Syst, 9(4): 1994–2006

Ye H, Guo H, Liu G, Ren Y, Ding Y, Lv M (2016). Coverage analysis on global change sensitive regions from lunar based observation. IEEE Int Geosci Remote Sens Symp: 3734–3737

Yu C 2012. Study on characteristics of electromagnetic waves propagating through ionosphere and microwave absorbing properties of carbonaceous materials. Dissertation for Ph.D Degree. Nanjing: Nanjing University of Information Science and Technology (in Chinese)

Yujiri L, Fornaca S W, Hauss B I, Kuroda R T, Lai R, Shoucri M (1999). 140-GHz passive millimeter-wave video camera. Proc SPIE, 3364: 20–27

Yujiri L, Shoucri M, Moffa P (2003). Passive millimeter wave imaging. IEEE Microw Mag, 4(3): 39–50

Zhang C, Wu J (2007). Image simulation for ground objects microwave radiation. J Electr Inf Technol, 12(4): 750–764 (in Chinese)

Zhang D W 2012. Study on Moon-Earth observation methodology for global change Dissertation for Ph.D Degree. Shanghai: East China Normal University (in Chinese)

Zhang G, Zhang Z, Guo W (2003). 8 mm radiometric simulation detection based on optical image. Int J Infrared Millim Waves, 24(4): 603–611